Chemical Engineering Science 259 (2022) 117731

Contents lists available at ScienceDirect

Chemical Engineering Science

journal homepage: www.elsevier.com/locate/ces

Investigating the effects of helium, argon and hydrogen co-feeding on the non-oxidative coupling of methane in a dielectric barrier discharge reactor

Pierre-André Maitre, James Long, Matthew S. Bieniek, Marcus N. Bannerman, Panagiotis N. Kechagiopoulos *

Chemical Processes & Materials Group, School of Engineering, University of Aberdeen, Aberdeen, UK

HIGHLIGHTS

- Non-thermal methane plasma kinetic model accounts for Ar, He, and H_2 co-feeding.
- Reactivity and relaxation of excited states, and ions interactions are explicitly considered.
- Combined one and zero-dimensional modelling resolves wide range of time-scales.
- Argon promotes penning dissociations improving methane conversion energy efficiency.
- Hydrogen co-feeding increases ethane and ethylene selectivity versus acetylene.

GRAPHICAL ABSTRACT

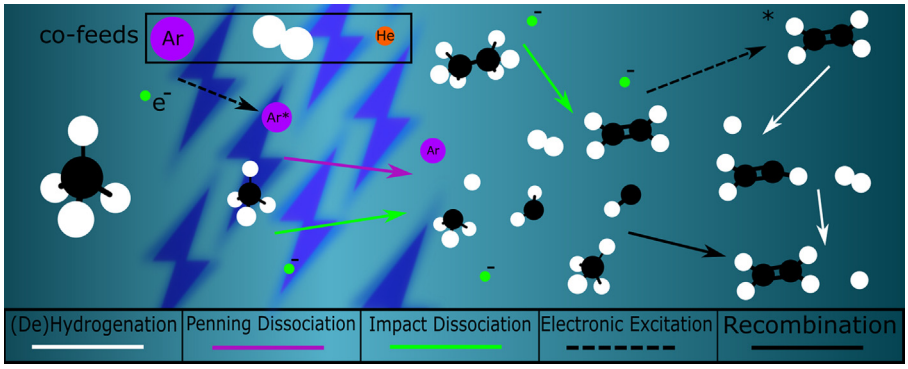

ARTICLE INFO

Article history:
Received 25 January 2022
Received in revised form 9 April 2022
Accepted 11 May 2022
Available online 23 May 2022

Keywords:
Methane valorisation
Non-thermal plasma reactor
Kinetic modelling
He, *Ar*, H_2 co-feeding

ABSTRACT

The impact of helium, argon, and hydrogen co-feeding on methane non-oxidative coupling in dielectric barrier discharges is investigated in terms of reaction pathways and energy efficiency. One-dimensional fluid simulations are used to investigate short time-scales. Zero-dimensional global modelling, using inputs from the one-dimensional simulations, is utilised to study time-scales equivalent to those of experimental reactors. A previously developed detailed kinetic scheme for non-thermal methane plasma that accounts for the reactivity and relaxation of electronically and vibrationally excited species is extended to describe the interactions of noble gases with the species within the methane plasma. A wide range of compositions and applied voltages are studied to determine the conditions that improve the energy efficiency of methane conversion and the selectivity to value-added products. Penning dissociation has a significant impact in the case of mixtures with high content of argon, while hydrogen co-feeding increases selectivity towards ethane and ethylene versus acetylene.

1. Introduction

The imminent depletion of conventional oil requires finding alternative carbon sources for petrochemicals. The upgrading of methane into value-added compounds has been intensely studied in recent literature due to methane's wide availability from fossil

* Corresponding author.
E-mail address: p.kechagiopoulos@abdn.ac.uk (P.N. Kechagiopoulos).

https://doi.org/10.1016/j.ces.2022.117731
0009-2509/

natural gas (Zichittella and Pérez-Ramírez, 2021) and shale gas (Galadima and Muraza, 2016), and renewable biogas (Zhang et al., 2021). The very stable nature of the methane molecule, with a $C-H$ bond energy of 4.52 eV, generally necessitates the use of high temperatures (Huang et al., 2018) and/or the presence of a catalyst (Guo et al., 2014) for its activation via conventional thermal processes. Although, the use of plasma for methane's activation has been under research for years, resulting even in commercial applications as early as the 1940s (Heinz, 1962), it has recently sparked renewed interest due to the aforementioned oil depletion and increasing climate change awareness. In such processes, the naturally present electrons in the gas bulk are accelerated by an externally applied field which leads them to collide with the methane molecules (Fridman, 2012). Upon collision, the methane molecules are ionised, increasing the population of electrons further via the so-called electron avalanche (Fridman, 2012). A variety of self-sustained electrical discharges can be created and operated at various pressure and temperature conditions and degrees of deviation from thermodynamic equilibrium (Scapinello et al., 2017). Furthermore, electron collisions can also dissociate methane, initiating reactive pathways that ultimately lead to the formation of higher carbon-number products (Maitre et al., 2020).

Co-feeding other gases can be used to facilitate methane's activation in plasma. In conventional thermal–catalytic processes, an oxidant (H_2O and CO_2 for the cases of steam and dry reforming or O_2 in partial oxidation and oxidative coupling processes) is typically mixed with methane at high temperature and in the presence of a catalyst to facilitate activation of the $C-H$ bond and reduce the formation of carbonaceous deposits on the catalyst. The equivalent plasma-activated processes have attracted the attention of the research community in recent literature (Sheng et al., 2020a; Sheng et al., 2020b; Sheng et al., 2018; Khoja et al., 2018; Khoja et al., 2019). However, the use of oxidants unavoidably leads to the creation of non-selective products that require either separation or further reactive steps to be upgraded.

The introduction of noble gases (He, Ne, Ar, Kr and Xe) has been considered in methane plasma-assisted combustion studies as a means to decrease the electric energy requirements of the process, improve the homogeneity of the discharge and assist in sustaining the flame (Lefkowitz et al., 2015; Mao et al., 2019; Starikovskiy and Aleksandrov, 2013; Kosarev et al., 2008; Aleksandrov et al., 2009; Sun et al., 2012). Noble gases have also been utilised in reactive plasmas as methane activation agents. Jo et al. (2013) investigated the impact of Ar, He and Ne addition on methane non-oxidative coupling in a double sided dielectric barrier discharge (DBD) reactor, further extending the study to Kr and Xe in Jo et al., 2014 and O_2 and Ar in Jo et al., 2015. Kundu et al. (2012) investigated the utilisation of quartz and alumina as dielectrics in Ar diluted methane plasma. Barni et al. (2019) studied experimentally and numerically the cracking of methane using a pulsed DBD diluted in Ar streams, whilst Sun and Chen (2019) investigated the role of He excitation on methane pyrolysis in a radio-frequency plasma. Finally, Huang et al. (2020) analysed both numerically and experimentally the feasibility of methane activation at low temperature using a nanosecond pulsed plasma in the presence of Ar and in the absence of a catalyst. In all the aforementioned works, it was suggested that the electronically excited states of the noble gases could induce Penning ionisation and dissociation that led to enhanced methane conversion and improved energy efficiency.

Mixtures of methane and hydrogen are often used in carbon vapour deposition for the synthesis of diamond (Sedov et al., 2020; Bolshakov et al., 2020; Ivanov et al., 2016) and their kinetics in microwave discharges have been the object of rigorous investigations (Gordon et al., 2001; Hassouni et al., 1998; Hassouni et al., 2006; Prasanna et al., 2017; Hassouni et al., 2001; Hiramatsu et al., 2003). Recently, experimental work from Scapinello et al. (2018, 2019) studied such mixtures in non-catalytic reactors with thermal discharges at various pressure ranges for the non-oxidative conversion of methane, finding high selectivities towards ethylene (the highest-value C_2 product of methane coupling). Hydrogen has also been introduced in catalytic reactors for methane upgrading processes as a coke-suppression agent in the work of García-Moncada et al. (2020). A similar approach was followed by Dinh et al. (2019) who studied the conversion of methane into acetylene using low-current arcs and Wnukowski et al. (2021) who studied the influence of hydrogen addition on methane coupling in a moderate pressure microwave plasma.

The majority of previous modelling works have focused on the study of short time-scale plasma events, while clearly performance at reactor time-scales is of critical need of investigation to enable the optimisation of real systems. Moreover, a range of studies in experimental literature, particularly on plasma-catalysis, consider noble gases within methane plasmas as inert diluents, although the presence of these species clearly affects energy channelling and overall reaction pathways. In the current work, a systematic study of the effect of noble gases and hydrogen addition at relevant time-scales of experimental reactors is carried out to determine the conditions under which the co-feeding of such gases can be beneficial to the non-catalytic methane non-oxidative coupling in terms of energy efficiency and selectivities towards value-added products. To achieve this, a combined zero and one-dimensional modelling approach is used to resolve short time-scale events and describe longer time-scales of continuously operating reactors. A DBD reactor configuration is selected on account of the popularity of this discharge in plasma-catalysis and plasma-kinetics research, however the kinetic model developed can find application in a range of discharges and alternate processes with limited adaptations.

2. The model

The set of equations and methods applied in the current work follow those described in Maitre et al. (2021) and are only briefly recapped here. One-dimensional simulations across the electrode gap are performed to describe the behaviour of the DBD reactor in short time-scales. One-dimensional outputs, namely the time evolution of the averaged reduced field and electron density over a voltage period, are used as inputs for the zero-dimensional model to study the reactor performance at longer time-scales. For the case where methane is mixed with hydrogen, simulations are run at different initial CH_4/H_2 ratios using the kinetic scheme presented in Maitre et al. (2021). For the cases where Ar or He are co-fed, this comprehensive scheme is further expanded to account for the creation of ions and excited states originating from the noble gases and to describe the interactions of these species with those of the methane scheme.

2.1. Species addition

Due to the non-reactive nature of the noble gases, the species needed to be added to the pure methane scheme were limited. These included the ground states (Ar or He), one positive ion per species and several electronically excited states (see Table 1). The selection of excited states was based on the availability of electron collision cross-section data in the LXCat database (Pancheshnyi et al., 2012).

Table 1
Species added to the pure methane kinetic scheme presented in Maitre et al. (2021) to account for the presence of *Ar* and *He* noble gases within the plasma.

CH_4/Ar scheme	CH_4/He scheme
Ar, Ar^+, $Ar^*(11.55\ eV)$, $Ar^*(13.00\ eV)$, $Ar^*(14.00\ eV)$	He, He^+, $He^*(19.82\ eV)$, $He^*(20.61\ eV)$

2.2. Processes addition

To account for the presence of *Ar* or *He* in methane plasma, a set of 44 and 37 processes were added to the kinetic scheme from Maitre et al. (2021), respectively, and are briefly described below. Further details on the processes and the calculation of their reaction rate constants are given in the supplementary material (parts 1–5).

2.2.1. Electron collisions and electron-ion recombinations

Electron impact ionisations are included per ground state to form Ar^+ and He^+. Electronically excited states shown in Table 1 are similarly formed through electron collisions with the respective ground states. Ionisation from electronically excited states is treated as in Maitre et al. (2021) by shifting the cross-section of the respective ground state by the threshold energy of the excited state in the direction of low energy. Elastic collisions are very important in noble gases in terms of energy consumption and are included in both schemes. Electron-ion recombinations leading to the formation of an electronically excited state are considered for both cases:

$$e^- + He^+/Ar^+ \rightarrow He^*/Ar^*$$

For the case of *He*, a similar process involving a third-body electron is also included according to Lefkowitz et al. (2015):

$$e^- + e^- + He^+ \rightarrow He^* + e^-$$

2.2.2. Penning ionisations and dissociations

A characteristic of noble gases is their capacity to ionise or dissociate other molecules by quenching their excited states (Lefkowitz et al., 2015; Fridman, 2012; Jo et al., 2013; Jo et al., 2014; Jo et al., 2015; Berry, 1974), according to processes such as:

$$He^*/Ar^* + CH_4 \rightarrow CH_4^+ + e^- + He/Ar$$

$$He^*/Ar^* + CH_4 \rightarrow CH_3 + H + He/Ar$$

These processes are not well documented in literature, hence they are only considered for the feed molecule CH_4 where rate coefficients are available.

2.2.3. Vibrationally excited states quenching by He and Ar via Vibrational-Translational(VT) processes

The presence of noble gases in significant number densities requires accounting for the collisions between vibrationally excited states from the methane scheme (hydrocarbons and hydrogen) and *Ar* or *He* ground states. To this end, 15 Vibrational to Translational (VT) energy transfer processes were included per noble gas case. *Ar*/*He* diluted streams of methane have been reported to have longer relaxation times than pure methane ones (De Vasconcelos, 1976; De Vasconcelos and De Vries, 1977; Menard-Bourcin et al., 2005), as the smaller size of *Ar* and *He* in comparison to CH_4 induces less frequent collisions. Similarly to the approach followed in Maitre et al. (2021), experimental rate constants were used to describe these processes. Only in cases where experimental data were not available, the Lifshitz correlation was used to obtain an estimate of the rate constant (see supplementary material (part 5) and Maitre et al. (2021) for details).

2.3. Calculation domain of the 1D fluid model

Fig. 1 shows the geometry of the modelled DBD reactor. A double-sided arrangement consisting of 2 concentrically placed quartz tubes is considered with the ground electrode being located within the internal tube and the power electrode placed externally to the outer tube. In cylindrical coordinates, the calculation domain for the plasma spans across $R_{d1} : R_{d2}$, while the dielectric layers extend between $R_g : R_{d1}$ and $R_{d2} : R_e$ with $R_g = 0.5\ mm$, $R_{d1} = 1.5\ mm$, $R_{d2} = 3.5\ mm$ and $R_e = 4.5\ mm$.

The system of differential equations, comprising of species and electron density continuity equations along with the respective boundary conditions was implemented in the finite volume analysis software Plasimo (Dijk et al., 2009). More details and calculation procedures are presented in Maitre et al. (2021). To account for the effect of *He*, *Ar*, or H_2 co-feeding on transport properties, diffusion and mobility coefficients of all species were estimated for two limiting cases: full dilution in CH_4 and full dilution in the other considered species (*He*, *Ar* or H_2). A linear interpolation between these two limits was used to estimate coefficients for intermediate mixing ratios. Further details on transport coefficients can be found in the supplementary material (part 6).

3. Short time-scale results

Initially, the effect of methane's concentration in mixtures with helium, argon, and hydrogen on the electron temperature is studied using BOLSIG+ as a function of the reduced field (Fig. 2). For all co-feeding cases, higher electron temperatures are obtained for lower contents of methane. Noble gases, despite the high energy threshold of their first ionisation, are characterised by much lower breakdown voltages than molecular gases (Lieberman and Lichtenberg, 2005). This, seemingly contradictory, behaviour relates to the small size of their atoms, which results in longer electron mean free paths and less frequent electron collisions with heavy particles in noble gas plasmas in comparison to molecular ones. Consequently, the electrons are accelerated more by a given field and their temperature is higher. As evident in Fig. 2, helium, being the smallest element of those tested, shows overall the highest electron temperatures at equivalent concentrations. The trend is particularly visible for the 5% CH_4 case, with less variation compared to argon visible at higher methane contents. Interestingly,

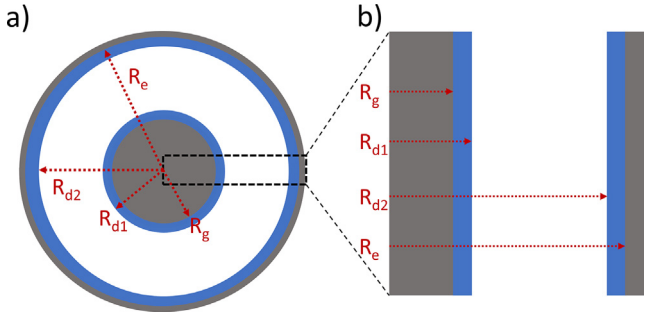

Fig. 1. Schematic of the double-sided dielectric barrier discharge reactor modelled. a) Cross-sectional view, b) Expanded view of the area outlined in the dashed black box, showing the computational domain of the 1D model. For both images the dielectrics are depicted in light blue and the electrodes in grey.

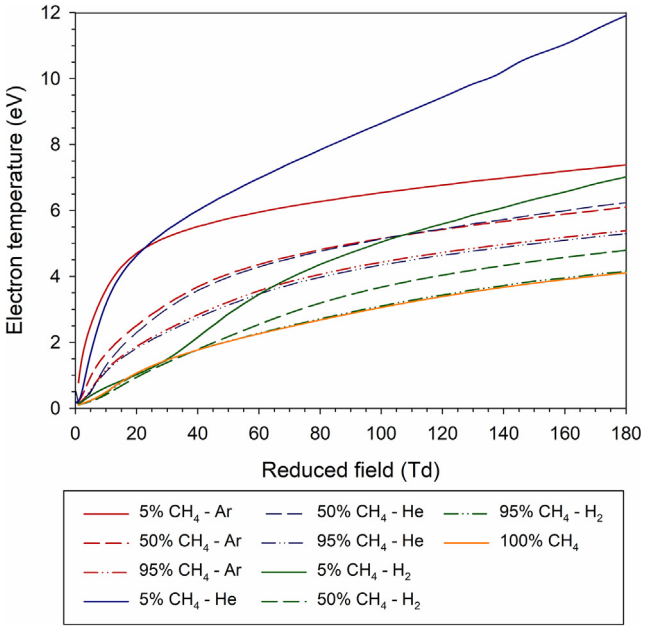

Fig. 2. Average electron temperature (eV) over reduced field (Td) for methane (yellow) and its mixtures with He (blue), Ar (red) and H_2 (green) obtained with BOLSIG+ using the cross-sections of the electron collision processes presented in the supplementary material (part 1) for He and Ar and in Maitre et al. (2021) for CH_4 and H_2.

though, even at 95% CH_4 concentration the electron temperature is enhanced by approximately 1.5 eV due to the presence of argon and helium compared to the 100% CH_4 case. Similar trends are observed during hydrogen co-feeding, as H_2 is the smallest existing molecular gas. Nonetheless, the effect is less pronounced, with the electron temperature reaching larger values than the pure methane case only at high hydrogen concentrations and at reduced fields above 40 Td.

The impact of co-feeding He, Ar or H_2 on the electron density and temperature of methane plasma is further investigated via one-dimensional simulations of the double-sided DBD reactor at different initial methane concentrations ranging from low (5% CH_4) to high (95% CH_4) and compared with the case of pure methane. All simulations are carried out at 25 kHz and for 0.2 ms (5 periods of the voltage). For the pure methane case, AC voltages of about 10 kV were necessary to ignite the plasma, while voltages as low as 4 kV were sufficient for methane streams highly diluted with He. The ability to ignite the plasma in methane mixtures at lower voltages than those for pure methane is potentially a means to reduce the energy requirements of the process. The applied voltage was hence varied from 10 kV down to 4 kV by increments of 2 kV for each dilution ratio and gas co-fed, but up to the lowest voltage that permitted ignition for a given ratio to avoid carrying out redundant simulations. The minimum voltage that was studied for each composition and gas co-fed is presented in Table 2.

At the short time-scales studied, the conversion of methane plasma is minimal (< 0.01%) and the main product is ethane for all cases. Focus is placed instead on the electron temperature and electron density, which vary the most at the simulated conditions. As can be observed in Fig. 3, the gas mixture composition has the largest impact on these variables, while points at different applied voltages are clustered around methane concentration level and the gas being co-fed. It is further seen that higher electron temperatures occur at lower electron densities and vice versa. This trend can be related to memory effects induced by the presence of positive ions. According to the one-dimensional simulations, the accumulation of ions at the dielectric interfaces facilitates the formation of electron streamers and the breakdown of the electric field at lower voltages. As a result, electrons are accelerated less and, hence, are colder on average when the influence of such memory effects is strong. This variation is evident in mixtures with Ar and He, as methane and other hydrocarbons are easier to ionise compared to noble gases and comprise the main source of positive ions. This phenomenon is also visible for hydrogen co-feeding, albeit to a lower extent. This is because hydrogen is a significant source of positive ions (H^+, H_2^+, H_3^+), and, even at high hydrogen content, the memory effect reduces the electron temperature significantly. This further explains the lower than average electron temperature in hydrogen mixtures in comparison to the other mixtures.

The averaged electron temperature and electron density ranges obtained are further compared with experimental atmospheric DBD literature. Using optical emission spectrometry, Barni et al. (2019) estimated an electron temperature of 2.5 ± 0.5 eV in both pure and 5% CH_4 mixtures in Ar in a pulsed DBD reactor, in good agreement with present results. Nonetheless, an electron density of approximately 10^{21} m^{-3} was derived in that work based on discharge current measurements, significantly higher than the results presented here, but consistent with the high energy densities observed in pulsed DBDs (Delikonstantis et al., 2020). Jo et al. (2013) reported averaged electron temperatures of 4.5 eV and 7.5 eV with an electron density of 4.7×10^{14} m^3 and 6.4×10^{14} m^3 in 10% mixtures of CH_4 in He and Ar, respectively, for a 3 mm DBD operated at 5 kV. Although the studied conditions are not identical, there are evident differences, e.g. to the $2 - 2.5$ eV electron temperatures and $< 3.0 \times 10^{17}$ m^{-3} electron densities obtained in this work for the 5% CH_4 in Ar and He cases (Fig. 3). The discrepancy most likely relates to the calculation method of the field followed by Jo et al., 2013. In that work, electron properties were obtained via BOLSIG+, using the bulk electric field approximation (Fridman, 2012), where the plasma's field, $E(t)$, is estimated using the experimental applied voltage, $V_{app}(t)$, and discharge gap, d, according to $E(t) \approx \frac{V_{app}(t)}{d}$. This approximation does not account for the field breakdown resulting from the opposite induced field created by the drift of charges. Consequently, the field is overestimated when averaged over time, further resulting in an overestimation of the electron temperature and an underestimation of the electron density.

The above highlight the advantage of using fluid models over bulk ones for the estimation of electron temperature and density, both variables that are of primary importance to reactive plasma processes for the calculation of the rates of the electron collisions. Nonetheless, the elucidation of the effect of the different diluents on methane conversion, product selectivities, and energy efficiency

Table 2
Minimum voltage (V) applied in the 1D simulations for the different initial methane concentrations (%) and gases co-fed.

Diluent	CH_4 fraction					
	5%	25%	50%	75%	95%	100%
He	4000	4000	6000	8000	8000	10000
Ar	6000	6000	8000	8000	10000	
H_2	6000	6000	8000	10000	10000	

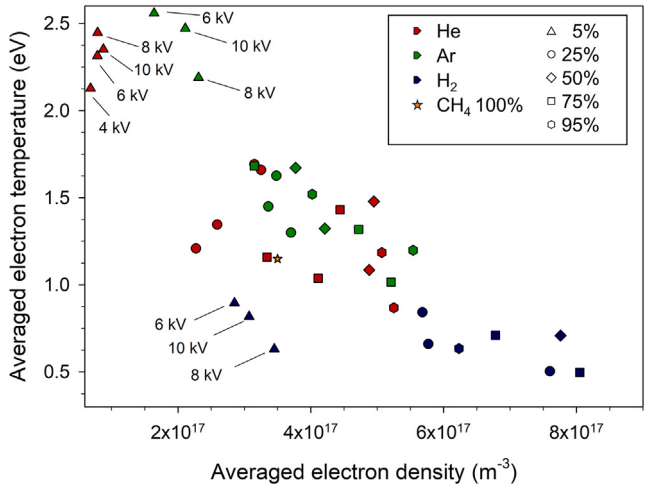

Fig. 3. Averaged electron temperature (eV) over averaged electron density (m^{-3}) obtained with the 1D fluid model for mixtures of methane with *He* (red), *Ar* (green) and H_2 (blue). The shape of the markers indicates the initial concentration of methane. Applied voltages are indicated only for 5% CH_4 mixtures for clarity.

requires the study of reactor performances at long time-scales, at prohibitive computational cost using fluid models. In the following, a hybrid zero and one-dimensional approach, as presented in Maitre et al. (2021), is used that combines the accuracy of the one-dimensional model for the estimation of electron properties with the computational efficiency of a zero-dimensional model.

4. Long time-scale results

Radially averaged values of the reduced field and electron density from the one-dimensional simulations for one voltage period are used as inputs into the zero-dimensional model according to Maitre et al. (2021). Zero-dimensional simulations are carried out varying the residence time, τ, (0.001, 0.01, 0.025, 0.05, 0.075 and 0.1 s) for each applied voltage value studied, gas co-fed and initial methane concentration level. Each case is simulated for a duration of five times the residence time, a period adequate for the continuous reactor to reach a periodic steady state, wherein the inputs of the one-dimensional simulations are repeated per applied voltage period.

4.1. Methane conversion

The reactor performance is analysed in terms of methane conversion, X_{CH_4}, calculated according to:

$$X_{CH_4} = \frac{n_{CH_4 feed} - n_{CH_4 lump}}{n_{CH_4 feed}} \quad (1)$$

where $n_{CH_4 feed}$ is the methane density in the feed stream and $n_{CH_4 lump}$ is the sum of the densities of the ground state methane and all of its excited states in the reactor:

$$n_{CH_4 lump} = n_{CH_4} + n_{CH_4(v2,4)} + n_{CH_4(v1,3)} + n_{CH_4^*(7.9eV)} \quad (2)$$

The specific energy density input (*SEI*) varies with the residence time and applied voltage, and is calculated by integrating the power density, P_d, across the residence time. The power density is obtained from:

$$P_d = e n_e v_e \frac{E}{N} \quad (3)$$

where n_e and $\frac{E}{N}$ are the radially averaged values of the electron density and reduced field from the one-dimensional simulations repeated during the zero-dimensional simulations, v_e is the electron velocity calculated during execution by BOLSIG+, and e is the elementary charge ($1.60217662 \times 10^{-19}\ C$). The specific energy

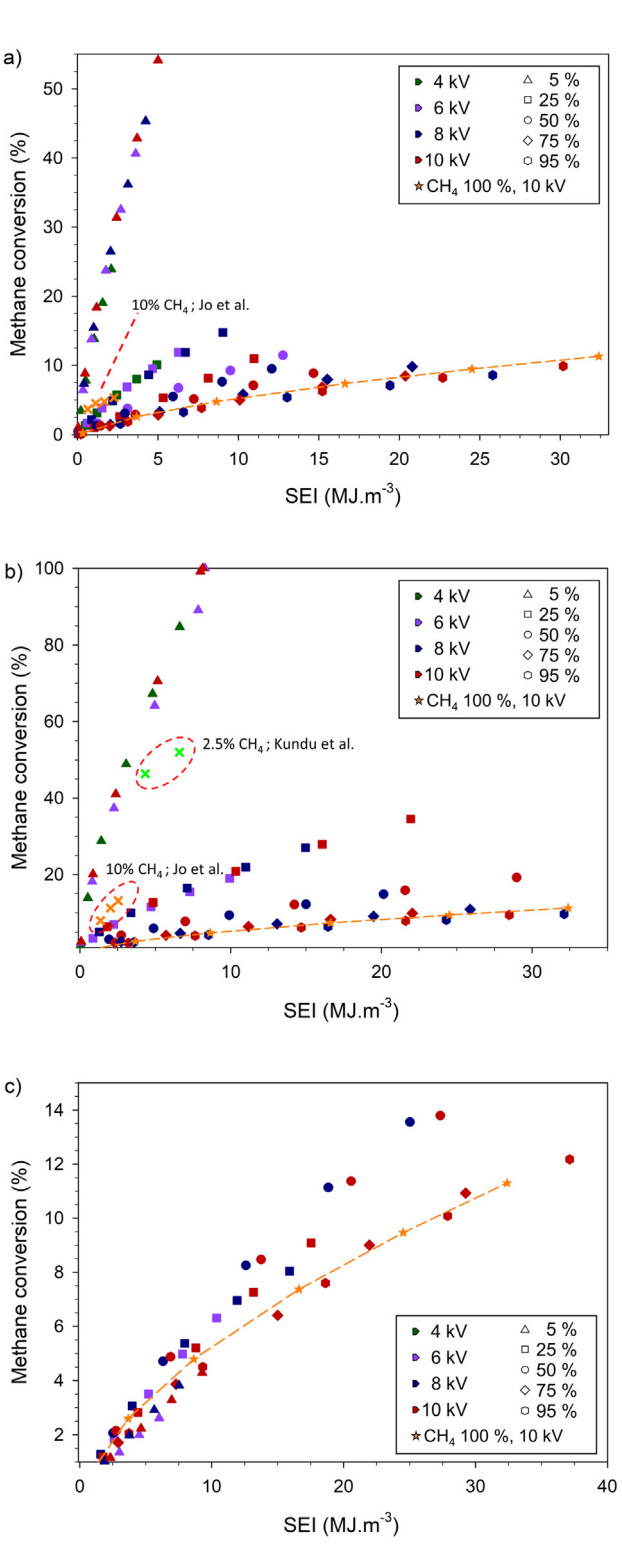

Fig. 4. Methane conversion (%) over *SEI* ($MJ.m^{-3}$) obtained with the 0D model for mixtures of methane with a) *He*, b) *Ar* and c) H_2. The colour of the data points denotes the applied voltage according to the first column solid pentagons of the legend. The shape of the data points denotes the dilution of methane according to the hollow shapes in the second column of the legend.

density input is estimated by dividing the integral of P_d across the whole simulation time (5τ) by five. The *SEI* calculated this way provides the total energy inputted into the reactor via electron processes per unit volume of the reactor, and varies linearly with the residence time.

Fig. 4 presents methane conversion against *SEI* for all cases simulated. Interestingly, data points for each methane mixture with *Ar* or *He* across all applied voltages and residence times studied follow clear linear trends in relation to *SEI* (Fig. 4-a and b). The effect of co-feeding on methane conversion is clearly visible for these gases, as the conversion values reached in low methane content simulations (5% and 25%) are up to 10 times higher than the base case of pure methane for the same residence times. Considering that these conversions are achieved on *SEI* ranges six and three times smaller for *He* and *Ar*, respectively, than pure methane, and for the same residence times, these results highlight the ability of noble gases to reduce the operational energy cost of the reactor. However, it is very important to note that the conversion increase in dilute streams is also due to the lower carbon content fed into the reactor, an aspect that is further investigated in Section 4.2.

Simulation results obtained with *Ar* in this work compare well with the experimental results obtained by Kundu et al. (2012), who reported methane conversions of 46.4% and 52.0% obtained at *SEI* values of 4.34 $MJ.m^{-3}$ and 6.60 $MJ.m^{-3}$, respectively, in an atmospheric DBD reactor at an applied voltage of 11 *kV* and a feed stream of 2.5% CH_4 in *Ar* (see Fig. 4-b). Similarly, Jo et al. (2013) reported methane conversions in the 4–7% range for *SEI* values between 0.714 $MJ.m^{-3}$ and 2.321 $MJ.m^{-3}$ for 10% CH_4 in *He* mixtures, and higher conversions of 8–14% for higher *SEI*s (1.4–2.5 $MJ.m^{-3}$) for 10% CH_4 in *Ar* mixtures, both observations aligning well with qualitative trends of this work (Figs. 4-a and b).

Hydrogen co-feeding has the smallest impact on methane conversion, with only the 50% mixture exhibiting a substantial increase at 8 and 10 *kV* in comparison to the pure methane case. For the 5% CH_4 mixture, the conversion is even below that of pure methane at an equivalent *SEI*, a behaviour mainly attributed to the lower electron temperature of this case discussed in the previous section, that is associated with reduced rates of electron collision processes. Moreover, the increased presence of *H* radicals enhances the rate of CH_3 conversion to methane (discussed in detail in Section 4.4.3).

The above trends are in qualitative agreement with the experimental observations of Scapinello et al. (2018). That work was performed with a nanosecond pulsed discharge, operated at much higher *SEI*, prohibiting a quantitative comparison. Nonetheless, it is noteworthy that the authors reported a 10% increase of methane conversion for a 50% CH_4 mixture with H_2 compared to the pure methane case (attributed to the higher energy amount channelled into the plasma) and a 20% decrease in methane conversion for 25 and 33% CH_4 mixtures in H_2.

Finally, no clear effect of applied voltage on the efficiency of the conversion can be discerned for any of the mixtures studied, as higher applied voltage leads to a concurrent increase of *SEI* and methane conversion. To account for the effect of dilution on energy efficiency, the amount of energy consumed per methane molecule is considered in the following section.

4.2. Energy efficiency and energy channelling

To account for the amount of methane molecules that are converted and the energy consumed in the various co-feeding cases studied, the energy efficiency, E_{eff}, of the process is defined. It is calculated by comparing the enthalpy of transformation of methane at 300 *K* to the cost of converting a methane molecule:

$$E_{eff} = 100\frac{\Delta H^{300K}_{equiv}}{E_{cost}} \tag{4}$$

E_{cost} $(eV.molecule^{-1})$ is calculated according to:

$$E_{cost} = \frac{SEI}{e\,(n_{CH_4feed} - n_{CH_4lump})} \tag{5}$$

while ΔH^{300K}_{equiv} is obtained from:

$$\Delta H^{300K}_{equiv} = \sum_{i}^{n_{prod}} S_i \Delta H^{300K}_{r}(i) \tag{6}$$

The above equation considers the composition of the different products that can result from the transformation of methane by weighting the enthalpy of each process with the selectivity of the corresponding product as obtained from the zero-dimensional simulations. The carbon-based product selectivities, $S_{C_xH_y}$, are calculated according to Eq. 7, where $n_{C_xH_y}$ refers to the density of any carbon containing species (molecules, radicals, ions), while for molecules that exist in different excited states a density lump $n_{C_xH_ylump}$ is considered, similar to the case of methane discussed earlier:

$$S_{C_xH_y} = \frac{x n_{C_xH_y}}{n_{CH_4feed} - n_{CH_4lump}} \tag{7}$$

The processes considered towards possible end products along with their enthalpy of reaction at 300 *K* are presented in Table 3.

Table 4 presents the respective energy efficiency results for the case of pure methane at 10 *kV*. E_{cost} overall increases with the rise in methane conversion and *SEI*, in agreement with Barni et al. (2019). E_{eff} remains extremely low as commonly reported for methane conversion in DBDs (SriBala et al., 2019), even in the presence of an oxidant (Snoeckx et al., 2013). The highest E_{eff} values are obtained for intermediate *SEI* cases studied (between 3.68 and 16.62 $MJ.m^{-3}$), due to the product selectivities obtained in that range. At low *SEI* and conversion, pure methane mainly transforms to ethane resulting to a low ΔH^{300K}_{equiv} (equivalent global process has the lowest reaction enthalpy). At higher conversions, the selectivity towards ethylene and acetylene becomes dominant, causing an increase of ΔH^{300K}_{equiv}, given the much higher reaction enthalpies of the respective global processes (Table 3).

To analyse the impact of co-feeding gases on energy efficiency, the respective E_{eff} data obtained are normalised in respect to those of the pure methane case at the same residence time (Fig. 5).

Helium is seen to have a positive impact on energy efficiency for methane contents lower than 50% for all applied voltages studied (Fig. 5-a). This improvement is a result of the higher electron temperature (as seen in Fig. 3) that enhances the rates of electron collisions with methane. Chemical interactions of excited helium with methane molecules are found to be negligible (elaborated in Section 4.4). The higher electron temperature observed for the 5% CH_4 case is even able to compensate for the significant fraction of

Table 3
Global processes considered and corresponding reaction enthalpies at 300 *K*.

Process	ΔH^{300K}_r $(kJ.mol^{-1})$	ΔH^{300K}_r (eV)
$CH_4 \rightarrow 1/2\ C_2H_6 + 1/2\ H_2$	33	0.342
$CH_4 \rightarrow 1/2\ C_2H_4 + H_2$	101	1.047
$CH_4 \rightarrow 1/2\ C_2H_2 + 3/2\ H_2$	188	1.949
$CH_4 \rightarrow 1/3\ C_3H_8 + 2/3\ H_2$	40	0.415
$CH_4 \rightarrow 1/3\ C_3H_6 + H_2$	82	0.850
$CH_4 \rightarrow C_{(s)} + 2\ H_2$	75	0.777

Table 4
Energy efficiency calculations for the pure methane case at 10 *kV*. Products selectivities discussed in Section 4.3.

$\tau\ (s)$	$SEI\ (MJ.m^{-3})$	$X_{CH_4}(\%)$	$E_{cost}\ (eV.molecule^{-1})$	$\Delta H^{300K}_{equiv}\ (eV.molecule^{-1})$	$E_{eff}(\%)$
0.001	0.33	0.22	37.97	0.45	1.18
0.01	3.68	2.56	36.08	0.81	2.23
0.025	8.65	4.79	46.06	1.02	2.20
0.050	16.62	7.37	57.51	1.17	2.04
0.075	24.51	9.46	66.06	1.26	1.90
0.1	32.40	11.29	73.12	1.31	1.80

energy that is lost in elastic collisions with *He* ($\approx 20-25\%$) (more details in supplementary material part 8). For mixtures with methane content equal to 50% and higher, the electron temperature is not high enough to enhance electron collision rates, hence the energy efficiency is either not significantly affected or becomes even worse than the case of pure methane at the same residence times. Overall, the generation of excited states from helium has minimal impact on the energy consumption as the energy fraction lost into their generation remains below 1% for all the cases considered (supplementary material part 8).

Argon has clearly a more positive effect on the energy efficiency in comparison to *He* (Fig. 5-b), in agreement with previous reports (Jo et al., 2013; Jo et al., 2014; Jo et al., 2015). This is especially true for mixtures below 50% CH_4 that are up to 4 times more energy efficient than the case of pure methane. This improvement is due to a combination of the higher electron temperature (especially for 5% methane, Fig. 3) and the facilitation of new methane activation channels by *Ar* excited states. Contrary to *He*, a significant part of the electrons' energy is channelled into the creation of excited states (supplementary material part 8), which contribute to the conversion of methane via Penning ionisations and dissociations (further discussed in Section 4.4). Energy efficiency for mixtures with a methane content higher than 50% is to a small extent lower than pure methane (Fig. 5-b), evidencing that at these concentrations the energy channelled into the excitation of *Ar* is not benefiting methane conversion.

Hydrogen co-feeding has a detrimental effect on the energy efficiency of methane conversion, with E_{eff} being lower for all cases studied in comparison to the equivalent pure methane values (Fig. 5-c). This is a consequence of the lower electron temperature that negatively impacts the conversion via electron collisions, despite the higher electron density seen in Fig. 3. Moreover, the presence of hydrogen is responsible for channelling most of the energy deposited into the electrons towards the creation of low reactivity vibrationally excited hydrogen species and towards non-reactive elastic collisions (supplementary material part 8). These results compare well with the experimental observations of Scapinello et al. (2018) who reported that the energy needed to convert 1 mol of CH_4 in 50%, 33%, and 25% mixtures of methane in hydrogen was 1.7, 4.7 and 6.2 times higher than that of the pure methane case at atmospheric pressure.

4.3. Selectivities of stable end products

The reactor performance is further analysed in terms of product selectivities. For all cases studied, the successive dehydrogenation of C_2 products with increasing methane conversion according to the general scheme $C_2H_6 \rightarrow C_2H_4 \rightarrow C_2H_2$ is evident, although at varying deviation from the pure methane case depending on the gas being co-fed. Hydrogen showed the most significant differences, with the respective C_2 products selectivities presented in Fig. 6. Equivalent results for *He* and *Ar* co-feeding are available in the supplementary material (part 9).

A clear increase in the selectivity towards ethane and ethylene is observed for intermediate compositions of H_2 (25% - 75% CH_4) in comparison to the pure methane case due to an enhancement of the hydrogenation of acetylene and ethylene. Producing more ethylene is desirable, as it is the highest value C_2 product. As discussed previously, H_2 co-feeding decreases the energy efficiency of methane plasma, hence the higher ethylene production could justify hydrogen's use. In the current model, the lowest energy cost achieved to produce one mole of C_2H_4 is 8743 $kJ.mol^{-1}_{C_2H_4}$, obtained for a ratio of 50% methane at 8 *kV*, which is in-line with the value of 6740 $kJ.mol^{-1}_{C_2H_4}$ that Scapinello et al. (2018) reported experimentally for the same composition, although in an atmospheric pressure pulsed discharge. These energy costs, however, are significantly higher to those obtained in plasma-catalytic reactors, as reported in the work of Delikonstantis et al. (2018) (1642 $kJ.mol^{-1}_{C_2H_4}$) or Wang and Guan (2016) (3266 $kJ.mol^{-1}_{C_2H_4}$).

Given the energy efficiency values obtained for the pure methane case (Table 4), it is not realistic to consider such a DBD-based process as a stand-alone industrial application. Nonetheless, the concurrent use of H_2 co-feeding to enhance the selectivity towards ethylene, and of *Ar* co-feeding to increase the energy efficiency of methane activation, appears to be able to lead to significantly lower cost of production of ethylene. When combined with a reactor that operates with renewable electricity at periods that production exceeds demand, there is prospect for the process finding application for the conversion of low-cost methane feedstocks, such as biogas and shale gas, to C_{2+}. H_2 to be co-fed could largely result from products separation, while *Ar* would similarly be separated and recycled. The use of an appropriate catalyst, however, appears to be the most feasible method to control the selectivity towards specific products, such as olefins (Scapinello et al., 2017).

4.4. Reaction pathway analysis

The impact of *He*, *Ar*, and H_2 co-feeding on the reaction pathways of the most important species (CH_4, C_2H_6, C_2H_4, C_2H_2 and H_2) are analysed here. An applied voltage of 10 *kV* with the reactor having reached steady-state is considered, resulting in methane conversions of 10% ($\pm$2%) for all the different compositions and gases studied. Similarly to the approach of Maitre et al. (2021), rates integrated over a simulated time of 0.2 *ms* (5 periods of the voltage) are considered and are presented as net production values in m^{-3}. In the following, only cases showing significant differences in the reaction pathways of pure methane are discussed. The complete reaction pathway analysis data for all gases co-fed and all products can be found in the supplementary material (part 10).

4.4.1. Co-feeding of helium

Co-feeding helium is found to have limited impact on the reaction pathway of methane non-oxidative coupling. For stable molecules, the relative contributions of the main processes are similar to those for the case of pure methane (supplementary material part 10 and Maitre et al. (2021)), so focus is placed on methane conversion pathways (Fig. 7).

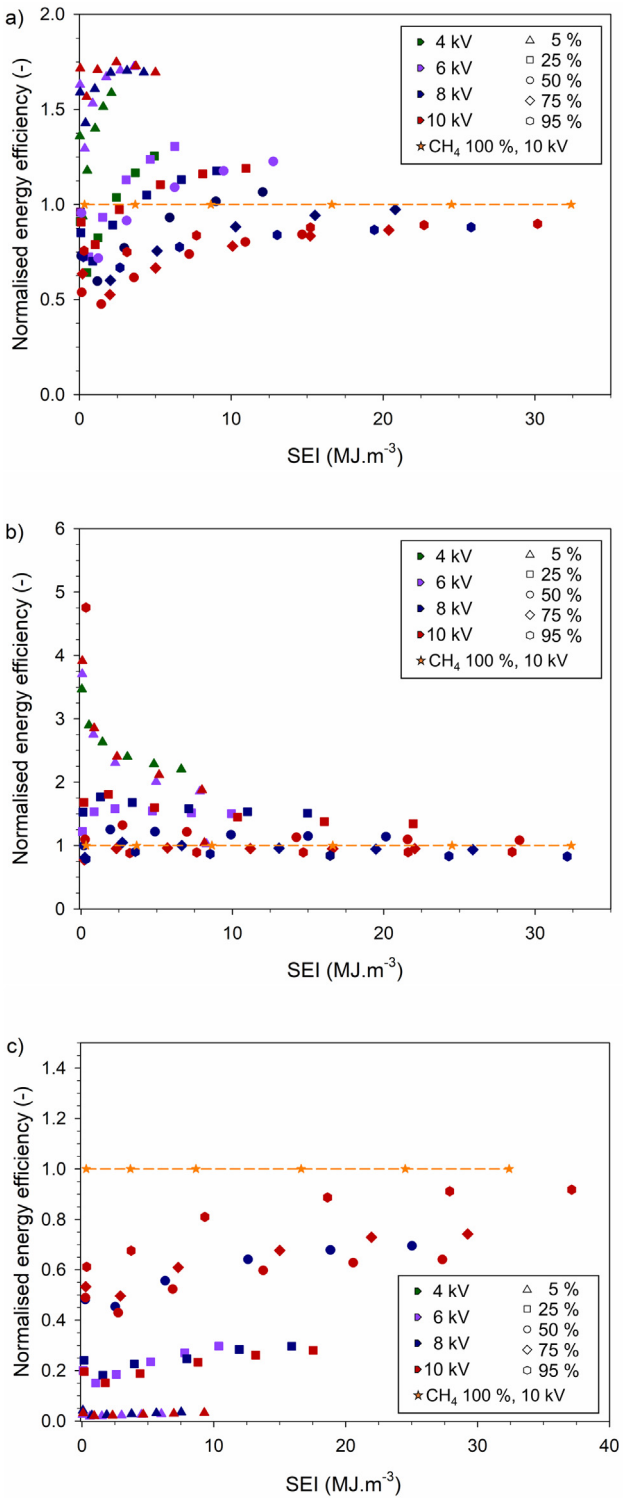

Fig. 5. Normalised energy efficiency (-) over *SEI* ($MJ.m^{-3}$), for mixtures of methane with a) *He*, b) *Ar* and c) H_2. The colour of the data points denotes the applied voltage according to the first column solid pentagons of the legend. The shape of the data points denotes the dilution of methane according to the hollow shapes in the second column of the legend.

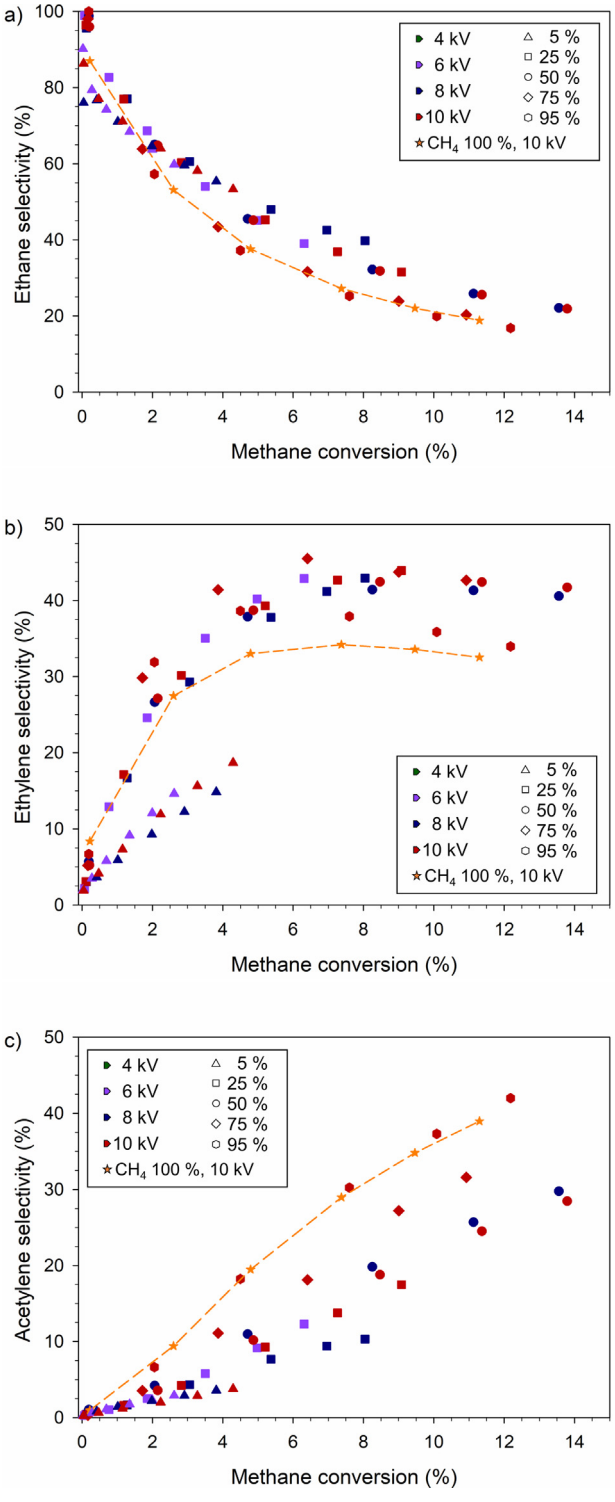

Fig. 6. a) Ethane, b) ethylene and c) acetylene selectivity (%) over methane conversion (%) obtained with the zero-dimensional model for mixtures of methane with H_2. The colour of the data points denotes the applied voltage according to the first column solid pentagons of the legend. The shape of the data points denotes the dilution of methane according to the hollow shapes in the second column of the legend.

The small cross sections of the two electronically excited states of helium considered in the model, $He^*(19.82\,eV)$ and $He^*(20.61\,eV)$, result in a reduced contribution of the respective electron collisions and the absence of Penning ionisation/dissociation involving them. These results further agree with the limited energy channelling into these modes that was discussed in Section 4.2. Consequently, the contribution of these species to methane activation is from negligible at high helium content (5% CH_4) to non-existent at higher methane content (> 50% CH_4) in

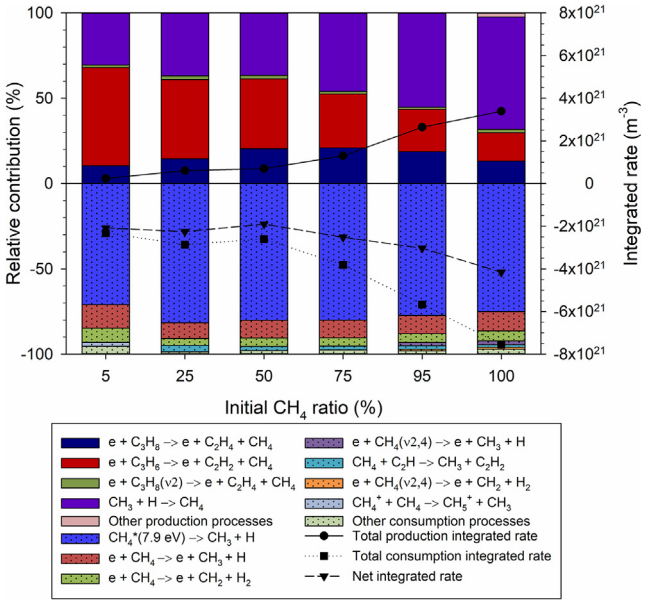

Fig. 7. Relative contribution (%) and integrated rate (net production in m^{-3}) over initial methane ratio (%) for the methane lump for $He - CH_4$ mixtures.

comparison to the dominant path of the self-dissociation of the electronically excited state $CH_4^*(7.9\,eV)$.

The higher electron temperature, observed at high helium content, enhances slightly electron collisions, with the vibrational and electronical excitations of methane and the first dissociation ($e^- + CH_4 \rightarrow e^- + CH_3 + H$) benefiting the most on account of their low energy thresholds. The contribution of vibrationally excited modes to the total methane lump conversion is low (< 1%); however, the enhancement of the direct dissociation and the self-dissociation of $CH_4^*(7.9\,eV)$ rates results in the low methane content cases (5 and 25 %) having a total net production of methane (integrated rate) approximately equal to the 50% case ($-2 \times 10^{22}\ m^{-3}$) (Fig. 7). For methane concentrations above 50%, the electron temperature is not high enough to enhance the electron processes; however, the increased concentration of methane ultimately leads to a rise (in absolute value) of the net production up to $-4 \times 10^{22}\ m^{-3}$ for the pure methane case.

4.4.2. Co-feeding of argon

Argon co-feeding has the most drastic impact on the energy efficiency of methane conversion due to the higher electron temperature it induces, as discussed for *He* too, but also because it enables the activation of methane by alternate pathways. The electronical excitation of *Ar* is much more feasible than that of *He* and is found to account for a significant fraction of the energy consumption (see Section 4.2). As a result, the quenching of argon's electronically excited states via the various Penning dissociation channels shown below becomes significant for methane concentrations below 50% (Fig. 8).

$$Ar^*(11.55\,eV/13.00\,eV) + CH_4 \rightarrow Ar + CH_3 + H$$

$$Ar^*(11.55\,eV/13.00\,eV) + CH_4 \rightarrow Ar + CH_2 + H_2$$

$$Ar^*(11.55\,eV/13.00\,eV) + CH_4 \rightarrow Ar + CH_2 + H + H$$

$$Ar^*(11.55\,eV/13.00\,eV) + CH_4 \rightarrow Ar + CH + H_2 + H$$

At higher methane content, the self-dissociation of $CH_4^*(7.9\,eV)$ and the first dissociation of methane by electron collisions remain dominant, as in the case of pure methane.

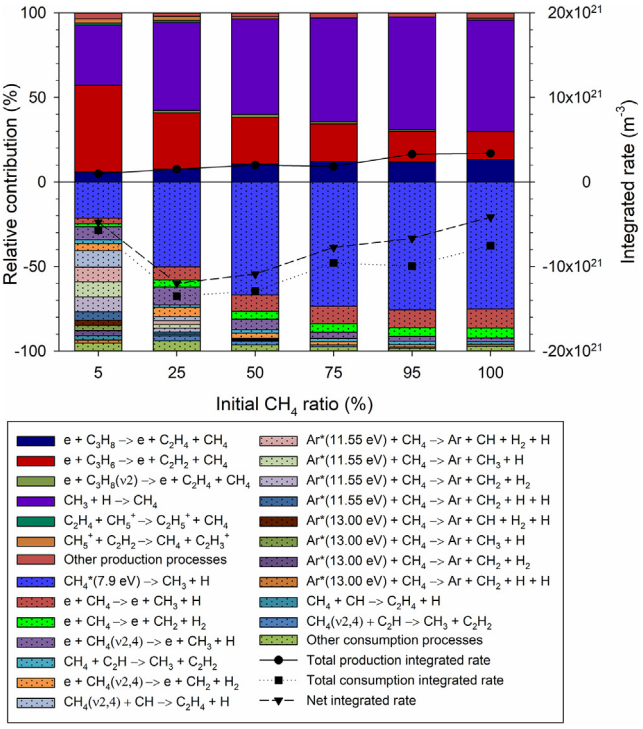

Fig. 8. Relative contribution (%) and integrated rate (net production in m^{-3}) over initial methane ratio (%) for the methane lump for $Ar - CH_4$ mixtures.

The relative importance of the lower energy vibrational mode of methane considered, $CH_4(v2,4)$, increases with *Ar* content. Collisions $e^- + CH_4(v2,4) \rightarrow e^- + CH_3 + H$ and $e^- + CH_4(v2,4) \rightarrow e^- + CH_2 + H_2$ are found to account for about 16% of methane's lump consumption at 5 and 25% CH_4 initial ratio in contrast to 9% at 50% CH_4 initial ratio, and below 5% for higher methane contents (Fig. 8). This enhancement is due to a density increase of $CH_4(v2,4)$ on account of the higher electron temperature, which promotes vibrational excitation, and an increased participation of the VT relaxation channel with *Ar* ($CH_4(v2,4) + Ar \rightarrow CH_4 + Ar$), which is two orders of magnitude slower than the equivalent process with CH_4.

At the studied conditions (10% conversion, 10 *kV*, 2 *ms* integration of the rates), the net consumption of methane is enhanced for all ratios studied in comparison to the 100% CH_4, which agrees with the higher energy efficiencies for all *Ar* co-feeding cases discussed in Section 4.2. The 5% CH_4 case exhibits faster rate of consumption of methane than the pure methane one, mainly due to Penning dissociations of argon's excited states (described above); however, the conversion is limited by the low density of methane. The highest methane net consumption with a value of $-1.2 \times 10^{22}\ m^{-3}$, three times faster than in pure methane plasma, is observed at the 25% CH_4 case (Fig. 8). The improved performance at this composition originates from a combination of positive effects arising from the presence of argon: higher electron temperature that enhances electron collision processes, higher presence of $CH_4(v2,4)$ thanks to slower relaxation, and a significant impact of the electronically excited states of argon. Indeed, at these conditions, 50.1% of methane's net consumption is due to the self-dissociation of $CH_4^*(7.9\,eV)$, 12.1% is due to the dissociation of CH_4 via electron collisions and 16.1% by the analogous dissociation process of $CH_4(v2,4)$, and 8.0% by Penning dissociations (Fig. 8). At higher methane content, the conversion slowly decreases as the positive effects of argon are diminishing.

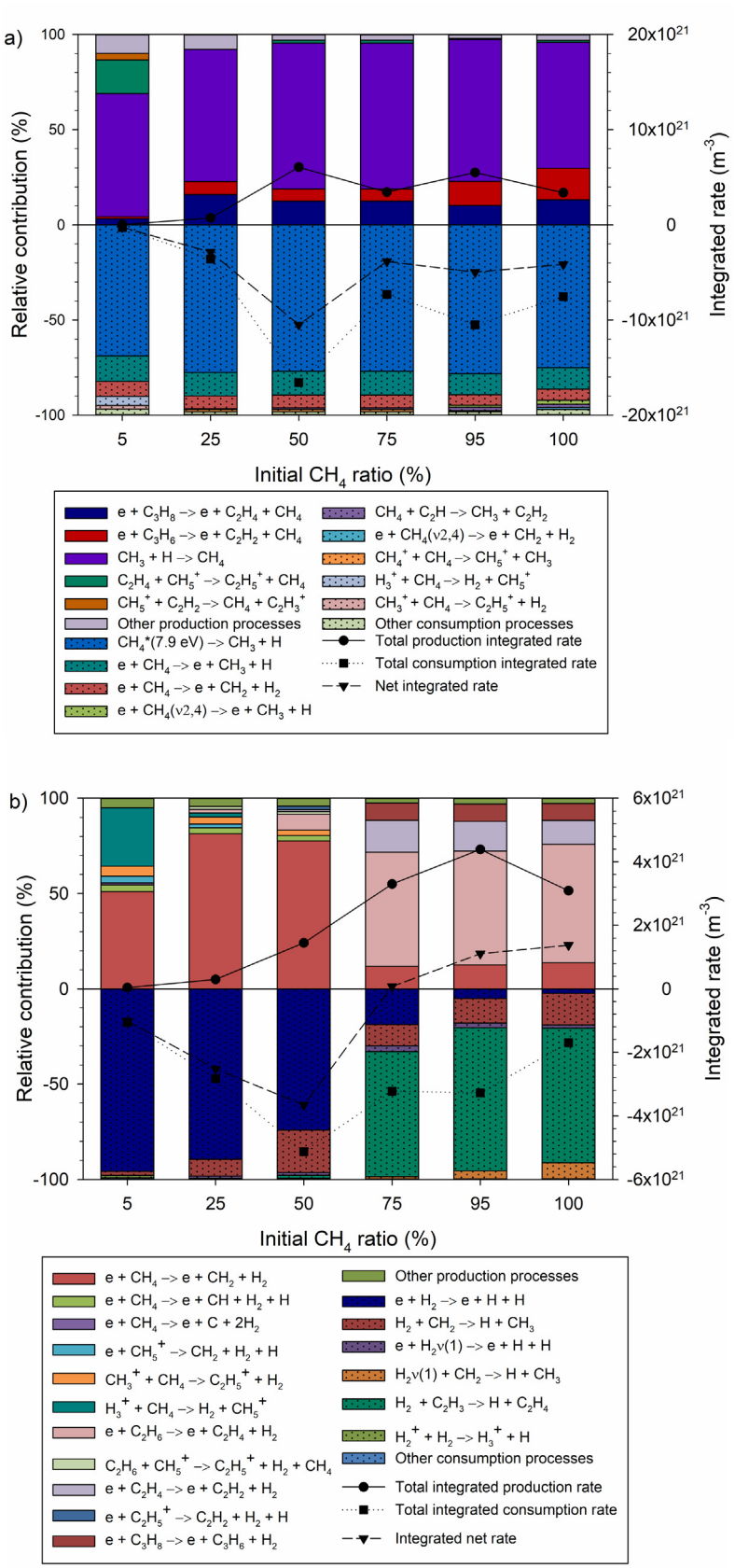

Fig. 9. Relative contribution (%) and integrated rate (net production in m^{-3}) over initial methane ratio (%) for $H_2 - CH_4$ mixtures for the a) methane lump and b) hydrogen lump.

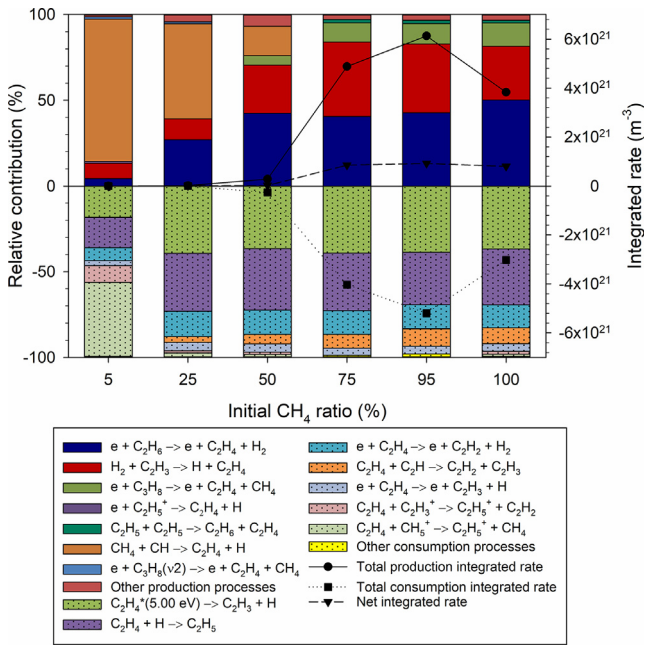

Fig. 10. Relative contribution (%) and integrated rate (net production in m^{-3}) over initial methane ratio (%) for $H_2 - CH_4$ mixtures for the ethylene lump.

4.4.3. Co-feeding of hydrogen

Hydrogen is the most reactive of all the gases studied and was discussed to enhance the production of ethane and ethylene in Section 4.3. The reaction pathway analysis for methane and hydrogen are presented in Fig. 9, while Fig. 10 shows the same analysis for ethylene.

At low methane content ($\leq 25\%$) the net consumption of methane is minimal due to the low methane density and the high recombination rate of CH_3 and H, induced by the high population of H radicals that originate from the dissociation of H_2 by electron collisions (Fig. 9-b). The highest net methane consumption ($-1.05 \times 10^{22}\ m^{-3}$) is achieved at 50% CH_4 inlet concentration, whereas at higher concentrations values obtained are an order of magnitude lower ($-1.05 \times 10^{21}\ m^{-3}$), in-line with methane conversion trends discussed in Section 4.1. The different processes contributing to the consumption of methane are overall similar for all inlet ratios studied and to those over pure methane, with the self-dissociation of $CH_4^*(7.9\ eV)$ accounting for about 75% of the total conversion and the dissociation of CH_4 by electron collisions for the rest. Contrary to what was observed with *Ar*, the vibrationally excited modes of methane are never populous enough to contribute significantly to the conversion of the lump (Fig. 9-a), due to their fast VT relaxation by H_2.

At methane ratios up to 50%, hydrogen acts as a co-reactant, as visible by its negative net production, which reaches a maximum (absolute) value of $-3.6 \times 10^{21}\ m^{-3}$ for 50% methane inlet concentration (Fig. 9-b). At higher methane contents, a positive net production of hydrogen production is observed, which, at the simulated conditions, is seen to take place primarily via ethane electron collisions towards ethylene (Fig. 9-b):

$$e^- + C_2H_6 \rightarrow e^- + C_2H_4 + H_2$$

In parallel, the primary consumption channel of ethylene, the self-dissociation of the electronically excited state $C_2H_4^*(5.0\ eV)$ towards C_2H_3:

$$C_2H_4^*(5.0\ eV) \rightarrow C_2H_3 + H$$

is counterbalanced by the fast hydrogenation of C_2H_3 radicals:

$$H_2 + C_2H_3 \rightarrow C_2H_4 + H$$

which explains the enhancement of ethylene selectivity over the presence of hydrogen in comparison to the pure methane case (discussed in Section 4.3).

These observations are confirmed by the RPA results of ethylene presented in Fig. 10. At low methane content (< 50%), the production of ethylene is minute and takes place mainly via the direct recombination of methane with *CH*:

$$CH_4 + CH \rightarrow C_2H_4 + H$$

At methane concentrations higher than 50%, the density of ethane becomes high enough to drive the production of ethylene. The slower ethylene dehydrogenation due to the presence of H_2 results in the highest net ethylene production of $9.26 \times 10^{20}\ m^{-3}$ at 75% initial methane ratio, in line with the higher selectivities observed for that ratio in Section 4.3.

5. Conclusions

In this work, the addition of *He*, *Ar*, and H_2 was studied to determine their impact on the performance of non-oxidative coupling methane plasma reactors. A comprehensive kinetic scheme developed previously for methane plasma was extended to account for the presence of noble gases and their ions and electronically excited states. Quenching of electronically excited states, ion interactions, and vibrational relaxation processes were included to describe the interaction of the noble gases with methane within the plasma.

One-dimensional fluid simulations of a double-sided DBD reactor at various applied voltages and initial methane ratios revealed the potential of *Ar* and *He* to increase the electron temperature at low methane content. H_2, on the contrary, was found to reduce the electron temperature due to strong memory effects induced by hydrogen ions (H_3^+, H_2^+ and H^+) accumulating at the dielectric walls.

Using the electron density and reduced field profiles from the one-dimensional results, zero-dimensional long time-scale simulations at different residence times were carried out to compare the performance of gases co-feeding with experimental literature results. The results demonstrated the potential of *Ar*, and a lesser extent of *He*, to improve the energy efficiency of methane coupling due to the higher electron temperature they induce and, for the case of *Ar*, the activation of methane through Penning dissociations. Notably, the energy efficiency enhancement was not accompanied by a change in product selectivities. H_2 co-feeding, on the other hand, was found to decrease the energy efficiency of methane coupling due to its own vibrational excitation. However, it was also observed to increase ethylene selectivity by up to 30% for CH_4/H_2 ratios between 25 and 75%, in excellent agreement with experimental results.

Using H_2 co-feeding to increase the production of ethylene and *Ar* to increase the energy efficiency of methane activation could lead to significantly lower cost of production of ethylene from methane non-oxidative coupling by plasma. Nonetheless, even if a positive impact on the energy efficiency was observed, the latter still remains relatively low (< 10%); therefore plasma-catalysis appears to be more promising for the development of a competitive methane upgrading process.

Declaration of Competing Interest

The authors declare that they have no known competing financial interests or personal relationships that could have appeared to influence the work reported in this paper.

Acknowledgements

We acknowledge and greatly appreciate the assistance from Dr. Mihailova from Plasma Matters B.V. in working with the software Plasimo.

The work was supported by the UK Engineering and Physical Sciences Research Council (EPSRC) New Investigator Award, Grant No. EP/R031800/1. James Long was supported by a doctoral scholarship within the Leverhulme Centre for Doctoral Training in Sustainable Production of Chemicals and Materials (DS-2017-073).

Appendix A. Supplementary material

Supplementary data associated with this article can be found, in the online version, at https://doi.org/10.1016/j.ces.2022.117731.

References

Aleksandrov, N.L., Kindysheva, S.V., Kukaev, E.N., Starikovskaya, S.M., Starikovskii, A. Y., 2009. Simulation of the ignition of a methane-air mixture by a high-voltage nanosecond discharge. Plasma Phys. Rep. 35 (10), 867. https://doi.org/10.1134/S1063780X09100109.

Barni, R., Benocci, R., Spinicchia, N., Roman, H.E., Riccardi, C., 2019. An Experimental Study of Plasma Cracking of Methane Using DBDs Aimed at hydrogen Production. Plasma Chem. Plasma Process. 39 (1), 241–258. URL http://link.springer.com/10.1007/s11090-018-9940-0.

Berry, R.S., 1974. The Theory of Penning Ionization. Radiat. Res. 59 (2), 367–375. URL https://www.rrjournal.org/doi/abs/10.2307/3573984.

Bolshakov, A.P., Ralchenko, V.G., Shu, G., Dai, B., Yurov, V.Y., Bushuev, E.V., Khomich, A.A., Altakhov, A.S., Ashkinazi, E.E., Antonova, I.A., Vlasov, A.V., Voronov, V.V., Sizov, Y.Y., Vartapetov, S.K., Konov, V.I., Zhu, J., 2020. Single crystal diamond growth by MPCVD at subatmospheric pressures. Mater. Today Commun. 25, 101635. URL http://www.sciencedirect.com/science/article/pii/S2352492820326465.

De Vasconcelos, M.H., 1976. Vibrational relaxation times in methane: The optic-acoustic effect. Ph.D. thesis. University of Amsterdam.

De Vasconcelos, M.H., De Vries, A.E., 1977. Vibrational relaxation time measurements in CH_4 and CH_4-rare gas mixtures. Physica A 86 (3), 490–512. URL http://www.sciencedirect.com/science/article/pii/0378437177900917.

Delikonstantis, E., Scapinello, M., Stefanidis, G.D., 2018. Low energy cost conversion of methane to ethylene in a hybrid plasma-catalytic reactor system. Fuel Process. Technol. 176, 33–42. URL https://linkinghub.elsevier.com/retrieve/pii/S0378382018301590.

Delikonstantis, E., Scapinello, M., Van Geenhoven, O., Stefanidis, G.D., 2020. Nanosecond pulsed discharge-driven non-oxidative methane coupling in a plate-to-plate electrode configuration plasma reactor. Chem. Eng. J. 380, 122477. URL http://www.sciencedirect.com/science/article/pii/S1385894719318807.

Dijk, J.V., Peerenboom, K., Jimenez, M., Mihailova, D., Mullen, J.V.D., 2009. The plasma modelling toolkit Plasimo. J. Phys. D: Appl. Phys. 42(19), 194012. URL http://stacks.iop.org/0022-3727/42/i=19/a=194012.

Dinh, D.K., Lee, D.H., Song, Y.-H., Jo, S., Kim, K.-T., Iqbal, M., Kang, H., 2019. Efficient methane-to-acetylene conversion using low-current arcs. RSC Adv. 9 (56), 32403–32413. https://pubs.rsc.org/en/content/articlelanding/2019/ra/c9ra05964d.

Fridman, A.A., 2012. Plasma chemistry. Cambridge University Press, Cambridge.

Galadima, A., Muraza, O., 2016. Revisiting the oxidative coupling of methane to ethylene in the golden period of shale gas: A review. J. Ind. Eng. Chem. 37, 1–13. URL https://www.sciencedirect.com/science/article/pii/S1226086X16300429.

García-Moncada, N., Cents, T., van Rooij, G., Lefferts, L., 2020. Minimizing carbon deposition in plasma-induced methane coupling with structured hydrogenation catalysts. J. Energy Chem. http://www.sciencedirect.com/science/article/pii/S2095495620306380.

Gordon, M.H., Duten, X., Hassouni, K., Gicquel, A., 2001. Energy coupling efficiency of a hydrogen microwave plasma reactor. J. Appl. Phys. 89 (3), 1544–1549. URL https://aip.scitation.org/doi/abs/10.1063/1.1337593.

Guo, X., Fang, G., Li, G., Ma, H., Fan, H., Yu, L., Ma, C., Wu, X., Deng, D., Wei, M., Tan, D., Si, R., Zhang, S., Li, J., Sun, L., Tang, Z., Pan, X., Bao, X., 2014. Direct, nonoxidative conversion of methane to ethylene, aromatics, and hydrogen. Science 344 (6184), 616–619. URL https://science.sciencemag.org/content/344/6184/616.

Hassouni, K., Duten, X., Rousseau, A., Gicquel, A., 2001. Investigation of chemical kinetics and energy transfer in a pulsed microwave H_2/CH_4 plasma. Plasma Sources Sci. Technol. 10 (1), 61–75.

Hassouni, K., Leroy, O., Farhat, S., Gicquel, A., 1998. Modeling of H_2 and H_2/CH_4 Moderate-Pressure Microwave Plasma Used for Diamond Deposition. Plasma Chem. Plasma Process. 18 (3), 325–362. https://doi.org/10.1023/A:1021845402202.

Hassouni, K., Lombardi, G., Duten, X., Haagelar, G., Silva, F., Gicquel, A., Grotjohn, T. A., Capitelli, M., Röpcke, J., 2006. Overview of the different aspects in modelling moderate pressure H_2 and H_2/CH_4 microwave discharges. Plasma Sources Sci. Technol. 15 (1), 117–125.

Heinz, G., 1962. How huels makes acetylene by dc arc. Hydrocarb Process Pet Refin 41, 159–164.

Hiramatsu, M., Kato, K., Lau, C.H., Foord, J.S., Hori, M., 2003. Measurement of C_2 radical density in microwave methane/hydrogen plasma used for nanocrystalline diamond film formation. Diam. Relat. Mater. 12 (3), 365–368. URL http://www.sciencedirect.com/science/article/pii/S0925963502002169.

Huang, B., Zhang, C., Bai, H., Zhang, S., Ostrikov, K.K., Shao, T., 2020. Energy pooling mechanism for catalyst-free methane activation in nanosecond pulsed non-thermal plasmas. Chem. Eng. J. 396, 125185. URL https://linkinghub.elsevier.com/retrieve/pii/S1385894720311773.

Huang, K., Miller, J.B., Huber, G.W., Dumesic, J.A., Maravelias, C.T., 2018. A general framework for the evaluation of direct nonoxidative methane conversion strategies. Joule 2 (2), 349–365. URL https://www.sciencedirect.com/science/article/pii/S2542435118300011.

Ivanov, O.A., Vikharev, A.L., Gorbachev, A.M., 2016. Experimental study of plasma decay in pulsed microwave discharges of H_2, CH_4 and their mixtures. Plasma Sources Sci. Technol. 25 (3), 035017. https://doi.org/10.1088/0963-0252/25/3/035017.

Jo, S., Hoon Lee, D., Song, Y.-H., 2015. Product analysis of methane activation using noble gases in a non-thermal plasma. Chem. Eng. Sci. 130, 101–108. URL http://www.sciencedirect.com/science/article/pii/S0009250915001918.

Jo, S., Lee, D.H., Kang, W.S., Song, Y.-H., 2013. Methane activation using noble gases in a dielectric barrier discharge reactor. Phys. Plasmas 20 (8), 083509. URL https://aip.scitation.org/doi/10.1063/1.4818795.

Jo, S., Lee, D.H., Kim, K.-T., Kang, W.S., Song, Y.-H., 2014. Methane activation using Kr and Xe in a dielectric barrier discharge reactor. Phys. Plasmas 21 (10), 103504. URL https://aip.scitation.org/doi/10.1063/1.4897171.

Khoja, A.H., Tahir, M., Amin, N.A.S., 2018. Cold plasma dielectric barrier discharge reactor for dry reforming of methane over Ni/γ-Al_2O_3-MgO nanocomposite. Fuel Process. Technol. 178, 166–179. URL https://linkinghub.elsevier.com/retrieve/pii/S0378382018304739.

Khoja, A.H., Tahir, M., Saidina Amin, N.A., 2019. Process optimization of DBD plasma dry reforming of methane over Ni/$La_2O_3MgAl_2O_4$ using multiple response surface methodology. Int. J. Hydrogen Energy 44 (23), 11774–11787. URL https://linkinghub.elsevier.com/retrieve/pii/S0360319919310158.

Kosarev, I.N., Aleksandrov, N.L., Kindysheva, S.V., Starikovskaia, S.M., Starikovskii, A. Y., 2008. Kinetics of ignition of saturated hydrocarbons by nonequilibrium plasma: CH_4-containing mixtures. Combust. Flame 154 (3), 569–586. URL http://www.sciencedirect.com/science/article/pii/S0010218008000825.

Kundu, S.K., Kennedy, E.M., Gaikwad, V.V., Molloy, T.S., Dlugogorski, B.Z., 2012. Experimental investigation of alumina and quartz as dielectrics for a cylindrical double dielectric barrier discharge reactor in argon diluted methane plasma. Chem. Eng. J. 180, 178–189. URL http://linkinghub.elsevier.com/retrieve/pii/S1385894711014392.

Lefkowitz, J.K., Guo, P., Rousso, A., Ju, Y., 2015. Species and temperature measurements of methane oxidation in a nanosecond repetitively pulsed discharge. Philos. Trans. Roy. Soc. A: Math. Phys. Eng. Sci. 373 (2048), 20140333. URL http://rsta.royalsocietypublishing.org/lookup/doi/10.1098/rsta.2014.0333.

Lieberman, M.A., Lichtenberg, A.J., 2005. Principles of plasma discharges and materials processing. Wiley-Interscience, Hoboken, N.J.

Maitre, P.A., Bieniek, M.S., Kechagiopoulos, P.N., 2020. Plasma-enhanced catalysis for the upgrading of methane: a review of modelling and simulation methods. React. Chem. Eng. 5, 814–837. https://doi.org/10.1039/D0RE00024H.

Maitre, P.A., Bieniek, M.S., Kechagiopoulos, P.N., 2021. Modelling excited species and their role on kinetic pathways in the non-oxidative coupling of methane by dielectric barrier discharge. Chem. Eng. Sci. 234, 116399. URL https://www.sciencedirect.com/science/article/pii/S0009250920309313.

Mao, X., Rousso, A., Chen, Q., Ju, Y., 2019. Numerical modeling of ignition enhancement of CH_4/O_2/He mixtures using a hybrid repetitive nanosecond and DC discharge. Proc. Combust. Inst. 37 (4), 5545–5552. URL http://www.sciencedirect.com/science/article/pii/S154074891830107X.

Menard-Bourcin, F., Boursier, C., Doyennette, L., Menard, J., 2005. Rotational and Vibrational Relaxation of Methane Excited to 2 ν_3 in CH_4/H_2 and CH_4/He Mixtures at 296 and 193 K from Double-Resonance Measurements. J. Phys. Chem. A 109 (14), 3111–3119. URL https://pubs.acs.org/doi/10.1021/jp0448649.

Pancheshnyi, S., Biagi, S., Bordage, M., Hagelaar, G., Morgan, W., Phelps, A., Pitchford, L., 2012. The LXCat project: Electron scattering cross sections and swarm parameters for low temperature plasma modeling. Chem. Phys. 398, 148–153. URL http://linkinghub.elsevier.com/retrieve/pii/S030101041100139X.

Prasanna, S., Michau, A., Rond, C., Hassouni, K., Gicquel, A., 2017. Self-consistent simulation studies on effect of methane concentration on microwave assisted H_2-CH_4 plasma at low pressure. Plasma Sources Sci. Technol. 26 (9), 097001.

Scapinello, M., Delikonstantis, E., Stefanidis, G.D., 2017. The panorama of plasma-assisted non-oxidative methane reforming. Chem. Eng. Process. 117, 120–140. URL http://linkinghub.elsevier.com/retrieve/pii/S0255270116306870.

Scapinello, M., Delikonstantis, E., Stefanidis, G.D., 2018. Direct methane-to-ethylene conversion in a nanosecond pulsed discharge. Fuel 222, 705–710. URL http://www.sciencedirect.com/science/article/pii/S0016236118304071.

Scapinello, M., Delikonstantis, E., Stefanidis, G.D., 2019. A study on the reaction mechanism of non-oxidative methane coupling in a nanosecond pulsed discharge reactor using isotope analysis. Chem. Eng. J. 360, 64–74. URL https://linkinghub.elsevier.com/retrieve/pii/S1385894718323921.

Sedov, V.S., Martyanov, A.K., Khomich, A.A., Savin, S.S., Zavedeev, E.V., Ralchenko, V. G., 2020. Deposition of diamond films on Si by microwave plasma CVD in varied CH_4-H_2 mixtures: Reverse nanocrystalline-to-microcrystalline structure transition at very high methane concentrations. Diam. Relat. Mater. 109, 108072. URL http://www.sciencedirect.com/science/article/pii/S0925963520306257.

Sheng, Z., Kameshima, S., Sakata, K., Nozaki, T., 2018. Plasma-Enabled Dry Methane Reforming. In: Britun, N., Silva, T. (Eds.), Plasma Chemistry and Gas Conversion. IntechOpen. https://www.intechopen.com/books/plasma-chemistry-and-gas-conversion/plasma-enabled-dry-methane-reforming.

Sheng, Z., Kim, H.-H., Yao, S., Nozaki, T., 2020a. Plasma-chemical promotion of catalysis for CH_4 dry reforming: unveiling plasma-enabled reaction mechanisms. PCCP 22 (34), 19349–19358. URL https://pubs.rsc.org/en/content/articlelanding/2020/cp/d0cp03127e.

Sheng, Z., Watanabe, Y., Kim, H.-H., Yao, S., Nozaki, T., 2020b. Plasma-enabled mode-selective activation of CH_4 for dry reforming: First touch on the kinetic analysis. Chem. Eng. J. 399.

Snoeckx, R., Aerts, R., Tu, X., Bogaerts, A., 2013. Plasma-Based Dry Reforming: A Computational Study Ranging from the Nanoseconds to Seconds Time Scale. J. Phys. Chem. C 117 (10), 4957–4970. URL http://pubs.acs.org/doi/abs/10.1021/jp311912b.

SriBala, G., Michiels, D., Leys, C., Van Geem, K.M., Marin, G.B., Nikiforov, A., 2019. Methane reforming to valuable products by an atmospheric pressure direct current discharge. J. Cleaner Prod. 209, 655–664. URL http://www.sciencedirect.com/science/article/pii/S0959652618332256.

Starikovskiy, A., Aleksandrov, N., 2013. Plasma-assisted ignition and combustion. Prog. Energy Combust. Sci. 39 (1), 61–110. URL http://www.sciencedirect.com/science/article/pii/S0360128512000354.

Sun, J., Chen, Q., 2019. Kinetic roles of vibrational excitation in RF plasma assisted methane pyrolysis. J. Energy Chem. 39, 188–197. URL https://linkinghub.elsevier.com/retrieve/pii/S2095495618312002.

Sun, W., Uddi, M., Won, S.H., Ombrello, T., Carter, C., Ju, Y., 2012. Kinetic effects of non-equilibrium plasma-assisted methane oxidation on diffusion flame extinction limits. Combust. Flame 159 (1), 221–229. URL https://www.sciencedirect.com/science/article/pii/S0010218011002203.

Wang, B., Guan, H.M., 2016. Highly Efficient Conversion of Methane to Olefins via a Recycle-Plasma-Catalyst Reactor. Catal. Lett. 146 (10), 2193–2199. https://doi.org/10.1007/s10562-016-1846-y.

Wnukowski, M., van de Steeg, A., Hrycak, B., Jasiński, M., van Rooij, G., 2021. Influence of hydrogen addition on methane coupling in a moderate pressure microwave plasma. Fuel 288, 119674. URL https://linkinghub.elsevier.com/retrieve/pii/S0016236120326703.

Zhang, K., Zhang, F., Wu, Y.-R., 2021. Emerging technologies for conversion of sustainable algal biomass into value-added products: A state-of-the-art review. Sci. Total Environ. 784, 147024. URL https://www.sciencedirect.com/science/article/pii/S0048969721020945.

Zichittella, G., Pérez-Ramírez, J., 2021. Status and prospects of the decentralised valorisation of natural gas into energy and energy carriers. Chem. Soc. Rev. 50, 2984–3012. https://doi.org/10.1039/D0CS01506G.